Optics & Laser Technology 203 (2026) 115810

Contents lists available at ScienceDirect

Optics and Laser Technology

journal homepage: www.elsevier.com/locate/jolt

Full length article

Touch localisation accuracy of OptoSkin optical tactile sensors fabricated from different light-guide materials

Aleš Zore[a,*], Julija Stopar[a], Andrejs Ogurcovs[b], Jelena Butikova[b], Ilze Aulika[b], Jorge Garcia[c], Sergio Cartiel[c], Adolfo Muñoz[c], Martin Laurenzis[d], Emmanuel Bacher[d], Marko Munih[a], Roman Kamnik[a]

[a] University of Ljubljana, Faculty of Electrical Engineering, Ljubljana, Slovenia
[b] Institute of Solid State Physics, University of Latvia, Riga, Latvia
[c] Department of Computer Science and Systems Engineering, University of Zaragoza, Zaragoza, Spain
[d] French-German Research Institute of Saint-Louis, Saint-Louis, France

HIGHLIGHTS

- A presentation of a novel optical principle for large area tactile sensing and a simple algorithm for tactile localisation calculation.
- An experimental setup and protocol for automated performance evaluation.
- A touch location accuracy and Field-of-View assessment comparison for three different optical media.
- A comparative study of touch localisation performance for optical media manufactured using three different manufacturing technologies.
- Recommendations for selecting optical materials and fabrication technologies for producing optical sensor surfaces of arbitrary shapes.

ARTICLE INFO

Keywords:
TIR
Localisation
Time-of-flight
LIDAR
Optical sensing
Robot skin
Touch detection

ABSTRACT

Providing feedback information on touch is crucial in human–robot collaboration tasks. Within the framework of the HE SestoSenso project, a novel approach to touch sensing was developed by exploiting the properties of laser beam propagation in light-guide materials, and three different prototype sensory surfaces were fabricated.

For the proposed OptoSkin robot-body optical sensor surface, which employs a time-of-flight (ToF) sensor combined with a light-guide material, a performance evaluation was conducted. Using a controlled test robot cell, two experiments were carried out: a field-of-view (FoV) assessment and a localisation accuracy evaluation. Three different prototypes made from optically transparent but distinct materials were examined: acrylic glass, a 3D-printed material, and soft silicone rubber.

The localisation evaluation was performed by applying controlled forces with a robot on a rectangular grid, with a raster spacing of 10 mm between individual touch locations. The evaluation results confirm accurate touch localisation, with an error of less than 5 mm and a variability of less than 2 mm in the sensor FoV. The comparison of the OptoSkin prototypes shows the best performance for the soft silicone rubber material and the worst for the 3D-printed material.

1. Background and introduction

Extensive touch, or tactile, perception opens a new dimension in robotics. Physical interaction with the environment is not only essential in social robotics but is also becoming increasingly important in industrial robotics, particularly in collaborative robotic tasks. It is no longer sufficient to merely detect whether contact has occurred; it is also necessary to determine where the contact took place, the magnitude of the applied force, and the extent of the interaction area between the robot and the object in contact.

The development and use of tactile sensors in robotics has a long history. There are several operating principles known, ranging from resistive, capacitive, magnetic, and optical approaches.

* Corresponding author.
Email addresses: ales.zore@fe.uni-lj.si (A. Zore), roman.kamnik@fe.uni-lj.si (R. Kamnik).

https://doi.org/10.1016/j.optlastec.2026.115810
Received 10 February 2026; Received in revised form 15 May 2026; Accepted 21 June 2026
Available online 30 June 2026
0030-3992/

Piezoresistive sensors and strain gauges (resistive sensors) measure changes in electrical resistance resulting from applied forces [1–3]. Resistive touch sensors offer high sensitivity at low cost, along with low noise and simple electronic design. However, nonlinear response, large hysteresis, and the need for complex circuitry remain their main drawbacks.

Magnetic sensors, also referred to as inductive sensors, measure changes in the amplitude and phase of a magnetic field [4]. Their main advantages include high sensitivity, wide dynamic range, minimal or no hysteresis, linear response, and strong physical robustness. However, their application is limited when interacting with nonmagnetic materials.

Capacitive tactile sensors estimate contact or proximity from changes in the electric field coupling between electrodes, commonly implemented as self-capacitance, mutual-capacitance, interdigitated, or deformable parallel-plate structures [5–9]. Their electrodes can be fabricated on flexible PCBs, textiles, or elastomeric substrates at small scales, enabling thin, lightweight, low-power, and spatially dense robotic-skin arrays [10–13]. Compared with resistive or piezoresistive skins, capacitive sensors generally offer better suitability for static-force measurement and lower power consumption. Their main challenge is sensing the small capacitance variation, often in the fF – pF range.

Optical sensors exploit the detection of changes in light intensity or in the spectral characteristics of the light source propagating through media with different refractive indices to estimate applied contact parameters [7]. They are immune to electromagnetic interference and can be highly flexible; however, optical losses may distort the measured signal.

A key advantage of optical sensors is that large areas can be sensorised without the need to wire each individual taxel (tactile sensing unit). Moreover, optical sensing approaches are particularly promising for covering extended surfaces with lower spatial resolution or larger taxel spacing.

One of the optical methods for touch and pressure detection exploiting light propagation behaviour is Frustrated Total Internal Reflection (FTIR). This method relies on total internal reflection of infrared light within an optically transparent medium until an external object interferes with the surface [14–17]. When an external object establishes contact with the surface of the light-guide medium, light partially escapes and changes. The applied pressure either alters the local refractive index or reduces the angle of incidence below the critical angle, causing light to scatter at the contact point. From the reflected light, information about the contact parameters can be extracted.

In most FTIR applications, multiple light transmitters and receivers are required to cover larger sensing areas. High sensitivity and the capability for simultaneous multi-touch detection make FTIR-based solutions promising for robotic applications. However, despite these advantages, FTIR sensors are sensitive to ambient and external light, which often necessitates a controlled environment or frequent calibration. More recently, Bacher et al. [18] introduced direct time-of-flight (ToF) LiDAR-based sensing as a novel extension of FTIR technology. The combination of FTIR and ToF enables faster response times, increased flexibility at lower integration costs, and improved adaptability to large, complex, and non-planar sensing surfaces.

This article evaluates the touch localisation accuracy of three different OptoSkin sensory surfaces based on FTIR principles. Three OptoSkin prototypes fabricated from optically transparent but distinct materials, i.e., acrylic glass, a 3D-printed material, and soft silicone rubber, are examined. Using a robotic test setup, two-stage experiments are conducted in a controlled environment. During the experiments, a robot manipulator performs controlled contacts between a test indenter and the optical surface at a mesh of predefined raster positions. In the first stage, the field of view (FoV) of the ToF sensor integrated into each prototype is assessed. In the second stage, the localisation accuracy of the sensory surface, considered as a measurement system, is evaluated.

2. Optical sensory touch surface – OptoSkin

OptoSkin is an optical sensory surface that exploits infrared (IR) light propagation within a light-guide material based on total internal reflection (TIR). A ToF sensor is positioned at the edge of the light-guide and emits IR light into the material, where it propagates by means of TIR. Ideally, the light reaches the end of the light-guide and is refracted back into the material, eventually returning to the ToF sensor [18] (see Fig. 1(a). The time of flight of the reflected signal is related to the effective length of the light guide. The reflected signal obtained in the absence of external contact is referred to as the baseline.

Several light-guide materials with different optical and mechanical properties were investigated, resulting in three OptoSkin prototypes manufactured using distinct fabrication processes. The first prototype employs commercially available rigid acrylic glass, while the second is based on a 3D-printed light-guide material; both are referred to as HardSkin. In contrast, the third prototype is fabricated from elastic silicone rubber (Crystalflex). The silicone rubber has a Shore A hardness of 20, corresponding to a compliance comparable to that of soft human skin, and is therefore referred to as SoftSkin.

The optical characteristics governing light propagation in the investigated light-guide materials–including transmittance T, diffuse reflectance R_d, scattering coefficient μ_s and refractive index n–measured over a spectral range of 175 nm to 3300 nm are listed in Table 1 [19].

Based on the physical properties of the light-guide material, two touch-sensing principles are possible. In OptoSkin, the light emitted by the ToF sensor propagates through the light-guide by means of total internal reflection (TIR), since $n_{\mathrm{OptoSkin}} > n_{\mathrm{air}}$ (Fig. 1a). When OptoSkin is touched, the light propagation is locally disturbed at the contact area due to interaction with the environment ($n_{\mathrm{environment}} \neq n_{\mathrm{air}}$). This disturbance occurs either through scattering caused by skin contact (FTIR, Fig. 1(b), when $n_{\mathrm{environment}} \approx n_{\mathrm{OptoSkin}}$, or through deformation of the

Table 1
Light-guide optical characteristics transmittance T, diffuse reflectance R_d, scattering coefficient μ_s and refractive index n in a spectral range of 175 nm to 3300 nm.

Light-guide material	T [%]	R_d [%]	μ_s [cm^{-1}]	n
Crystalflex	88.2	1.9	0.1	1.398
Acrylic glass	92.5	0.17	0.02	1.483
MonoCure3D Pro Crystal Clear 2	88.6	6.49	0.2	1.483

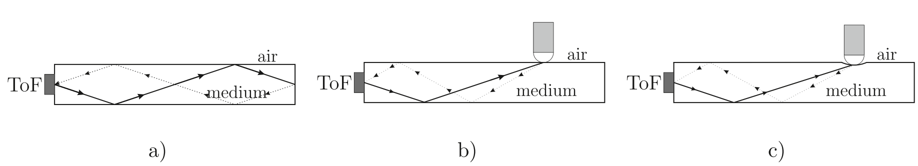

Fig. 1. OptoSkin touch detection working principle. a) total internal reflection - TIR within the light-guide medium, b) touch detection by frustrated total internal reflection - FTIR in a mechanically rigid medium (HardSkin), and c) deformation of the light-guide material in a mechanically soft medium (SoftSkin). The solid line represents the emitted light, while the dotted line represents the reflected light.

light-guide surface in the case of elastic materials (Fig. 1c). In the latter case, the condition for TIR, according to Snell's law and Fresnel formula [20], is only satisfied while the angle of incidence is bigger than the critical angle. Touch position is detected solely through FTIR in the acrylic glass and 3D-printed light-guide materials, and through a combination of FTIR and surface deformation in the elastic silicone rubber light-guide material.

FTIR in the case of HardSkin (acrylic glass and 3D-printed light-guide) results in a reduction in the relative refractive index (since the object has a higher refractive index than the light-guide), and the critical angle increases (therefore reducing the range of angles for total internal reflection). Additionally, in the case of SoftSkin, the geometry of the surface is changed, and surface normals are altered (pointing towards the sensor). In all cases, there is a minimal chance that light escapes from the light-guide before reaching the rear end of the light-guide material. With the ToF sensor's "vertical" FoV component of 52° and assuming the centre of the FoV is parallel to the edge of the light-guide, the minimum angle of incidence is going to be around 65° and is way beyond the critical angle for acrylic glass ($\Theta_c = 33.1°$, $n = 1.48$) and soft silicone rubber ($\Theta_c = 35.5°$, $n = 1.398$).

The operating principle of all three investigated prototypes is the same, with a ToF sensor placed at the edge of the light-guide material; however, their intended applications differ. Consequently, their physical dimensions, the number of embedded ToF sensors, and their placement also vary.

The configurations of OptoSkin prototypes are presented in Fig. 2. The acrylic glass HardSkin prototype has dimensions of 210 mm × 300 mm and a thickness of 3 mm. Two ToF sensors are embedded along the shorter sides, positioned off-centre with an offset of 130 mm from the corners and arranged opposite each other.

The soft silicone rubber SoftSkin prototype has the same planar dimensions as the acrylic glass HardSkin, with a thickness of 5 mm. Four ToF sensors are embedded along the two shorter sides, arranged as two opposing sensor pairs, as illustrated in Fig. 2(c). The 3D-printed HardSkin prototype has dimensions of 110 mm × 180 mm and a thickness of 5 mm. It incorporates two embedded ToF sensors positioned at the centres of the shorter sides, opposing each other (Fig. 2b).

Fig. 3 provides an overview of all physical prototypes. The acrylic glass HardSkin is shown in Fig. 3(a), the 3D-printed HardSkin in Fig. 3(b), and the soft silicone rubber SoftSkin in Fig. 3(c), all integrated within the robotic test setup.

Although individual prototypes incorporate multiple ToF sensors, in the analysis, only the responses of a single sensor per prototype were considered. Only in this manner could a sensor's FoV be evaluated. Selected ToF sensors for the individual prototype are coloured in red in Fig. 2. For acrylic glass and 3D-printed HardSkin, sensors on the lower sides were selected. For the soft silicone rubber SoftSkin, a right sensor on the lower side was selected. The responses obtained can then be mapped to the other sensors that were not directly measured and used to evaluate the responses of the entire OptoSkin sensor surface.

2.1. ToF sensor

All evaluated OptoSkin prototypes incorporate embedded AMS Osram TMF8828 ToF sensors. The TMF8828 is a single modular package

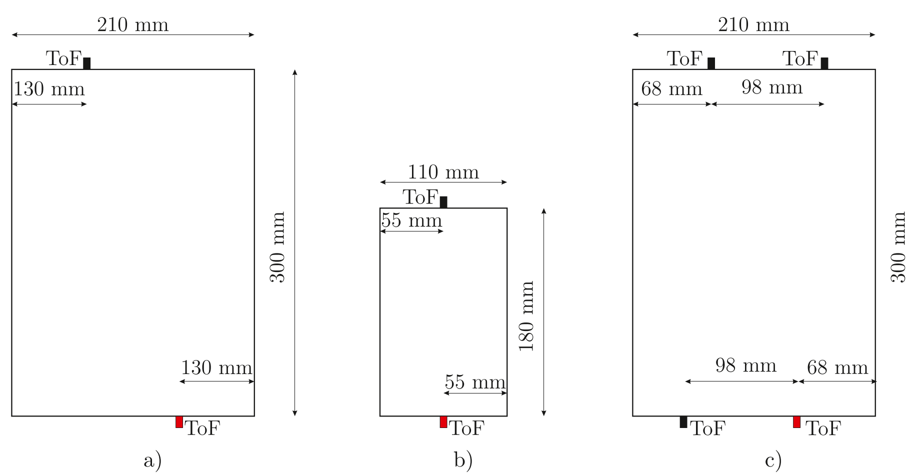

Fig. 2. Dimensions of the OptoSkin prototypes and ToF sensor positions. From left to right: a) acrylic glass HardSkin, b) 3D-printed HardSkin, and c) soft silicone rubber SoftSkin.

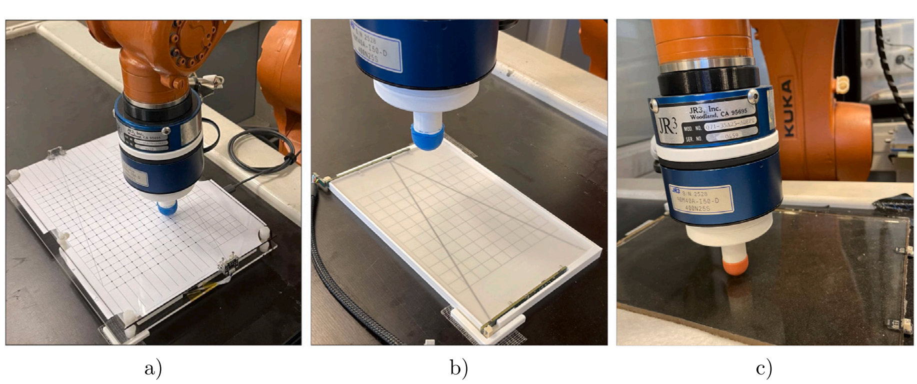

Fig. 3. OptoSkin prototypes integrated within the robotic test setup. From left to right: a) acrylic glass HardSkin, b) 3D-printed HardSkin and c) soft silicone rubber SoftSkin.

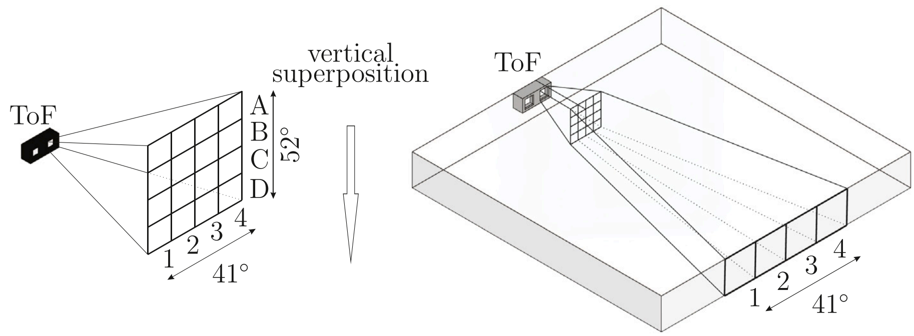

Fig. 4. Arrangement of SPADs in 4-by-4 mode for 3D spatial sensing and after vertical superposition for 2D planar sensing (ToF sensor embedded into medium).

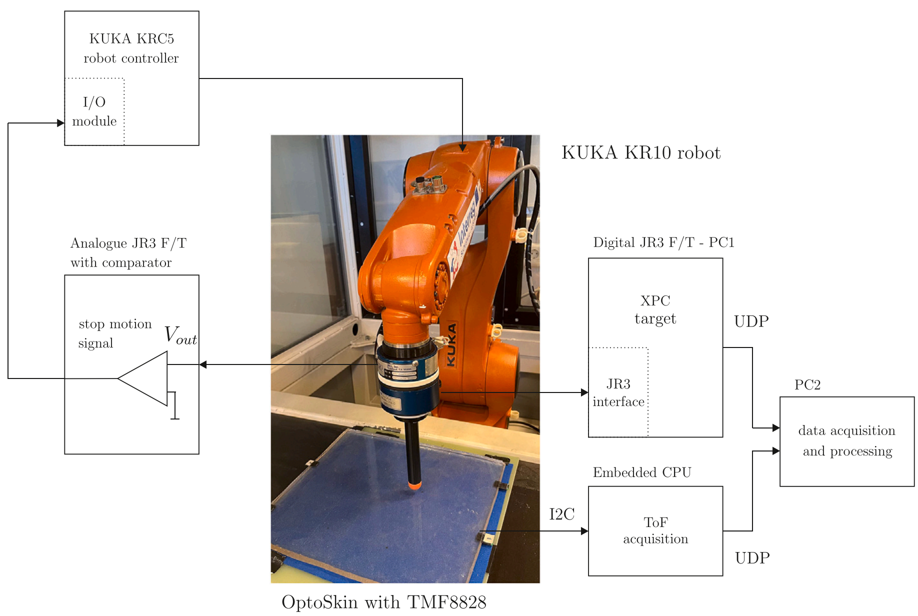

Fig. 5. Robot test setup for OptoSkin characterisation. The KUKA KR10 robot manipulator is used for indenter positioning and controlled force application on the OptoSkin surface. Two force/torque sensors, providing analogue and digital outputs, are employed for contact force acquisition.

that integrates a Vertical-Cavity Surface-Emitting Laser (VCSEL) and an array of 64 single-photon avalanche diodes (SPADs).

A multi-lens array provides a wide field-of-illumination (FoI) and field-of-view (FoV) of up to a maximum 63° diagonally or 41° × 52° (see Fig. 4, left). The sensor can operate in several predefined configurations, and by selecting different SPAD combinations, a sensor's effective FoV is determined, including 3-by-3 (33° × 32°), 3-by-6 (33° × 60°), 4-by-4 (41° × 52°), and 8-by-8 (41° × 52°) modes, as well as custom configurations.

One of the most beneficial properties of the sensor is its ability to output the temporal signal profile in histogram form. The VCSEL emits a pulse train, while the SPAD array receives the reflected light through the optical lens system. A time-to-digital converter (TDC) measures the time interval between emission and photon arrival. The TDC outputs a raw histogram representing the relationship between the number of detected photons and the corresponding time of flight. Access to this raw sensor data enables the implementation of custom algorithms for touch localisation.

The ToF sensor is originally intended for three-dimensional object sensing in free space; however, by directing the emitted light into a thin, optically transparent medium, the three-dimensional spatial sensing principle is effectively reduced to two-dimensional planar sensing. Consequently, the outputs from horizontal sensing layers are summed along vertically co-located elements, resulting in a single effective sensing layer. Fig. 4 illustrates the ToF FoV in free space when operating in 4-by-4 mode (left) and the corresponding reduction after embedding the sensor into the light-guide medium (right).

The ToF sensor was configured in an 8-by-8 mode for the acrylic glass HardSkin, in a custom 7-by-1 mode for the 3D-printed HardSkin, and in a 4-by-4 mode for the soft silicone rubber SoftSkin. The nominal FoV for the 8-by-8 and 4-by-4 modes is identical; however, the 8-by-8 mode provides higher spatial resolution, as it enables the acquisition of 64 histograms. The 7-by-1 mode has a nominal FoV 41° × 47°. Nevertheless, it allows data acquisition at a higher frame rate, since only seven SPADs (histograms) are read, and it also provides higher angular resolution compared with the 4-by-4 mode.

3. Methodology

The analysis of touch localisation for the OptoSkin sensory surfaces was conducted using a robotic test cell, as shown in Fig. 5. The experimental setup consists of a KUKA KR10 robotic arm equipped with two force/torque (F/T) sensors mounted in series on the end effector together with a custom-designed tool–indenter. The first F/T sensor (JR3 Q71-35A25-ADEPT), featuring an analogue output and an adjustable comparator, was used as a force-threshold trigger. The second F/T sensor (JR3 90M40A-I50-D), providing a digital output, was employed to measure the contact force applied by the robot.

The indenter design allows interchangeable tool tips with indenters of different shapes and sizes. For all subsequent localisation evaluation experiments, a rounded indenter with a diameter of 22 mm was used, approximating the dimensions of a human finger. The indenter was entirely fabricated from PLA using 3D printing and coated with a thin rubber layer, as contact with the PLA indenter alone does not elicit an FTIR response in the HardSkin prototypes.

The primary task of the robot is to ensure accurate positioning of the indenter on the OptoSkin surface and to apply the desired contact force by penetrating the OptoSkin material. Fig. 5 illustrates a schematic overview of the robotic test cell. The comparator output of the analogue F/T sensor is connected to a digital input of the robot controller and is set high when the applied force exceeds a predefined threshold, thereby stopping further penetration. The digital F/T sensor continuously transmits the measured force and torque data to a PC via the UDP protocol at a sampling rate of 100 Hz. The ToF sensor communicates with the OptoSkin acquisition system via the I^2C protocol, using an ESP32 microcontroller for both HardSkin prototypes and a Raspberry Pi 4B for the SoftSkin prototype. The acquisition system then transmits data packets via UDP to the data acquisition and processing PC, where online processing is performed within a MATLAB/Simulink model.

3.1. Empirical FoV assessment

Since the OptoSkin medium has a refraction index $n_{optoskin}$ different from that of air $n_{air} \approx 1$, the light emitted by the ToF sensor is refracted at the interface between the ToF sensor and the OptoSkin medium. As a result of $n_{\mathrm{OptoSkin}} > n_{\mathrm{air}}$, the effective FoV within the light-guide material is narrower than the nominal FoV specified in the sensor datasheet.

For each OptoSkin prototype, an empirical FoV assessment was conducted in the sensor's polar coordinate system. A robot executed 151 touch events along an arc at a radial distance r from the sensor, covering an angular range of $\pm 15°$ (i.e., 30° total) for the HardSkin prototypes and $\pm 20°$ (i.e., 40° total) for the SoftSkin prototype, with an angular resolution of $\Delta\Theta = 0.2°$. For the acrylic glass HardSkin and the soft silicone rubber SoftSkin, the radial distances were set to $r_1 = r_3 = 200$ mm, while for the 3D-printed HardSkin a shorter distance of $r_2 = 130$ mm was used. These differences in radial distances arise from variations in the physical dimensions of the OptoSkin prototypes. The arcs used for the empirical FoV assessment are illustrated in Fig. 6, where the sensor under evaluation is highlighted in red. All touch events for all three OptoSkin prototypes were performed with an applied normal force of $F = 30$ N.

The applied force threshold was set according to clinically examined regular pushes of the human finger (index finger and thumb) with either finger or whole palm contacts [21,22].

The primary objective of this test was to assess the effective FoV width, denoted as Θ_{FoV}. As a secondary outcome, the centres of the individual ToF sensor beams, labelled 1 to 4 in Fig. 4 for the 4-by-4 operating mode, were identified using best-fit Gaussian curves.

Prior to the FoV assessment measurements, a zero-state reference, referred to as the baseline acquisition, was recorded under no-touch conditions in order to capture the influence of temporal ambient light.

3.2. Experimental evaluation of touch localisation accuracy

For the evaluation of localisation accuracy, a rectangular grid of touch locations was defined for each OptoSkin prototype, accounting for differences in physical dimensions and ToF sensor placement. For the acrylic glass HardSkin, an 11×21 grid of touch points was designed with a 50 mm offset from the ToF sensor. For the 3D-printed HardSkin, an 11×13 grid with a 30 mm offset was used. Finally, for the soft silicone rubber SoftSkin, a 13×21 grid with a 50 mm offset from the ToF sensor was defined (see Fig. 7).

The touch points were defined on a uniform raster with a spacing of 10 mm between adjacent points. As in the FoV assessment, all touch events were performed by the robot with an applied normal force of $F = 30$ N.

For each predefined grid point, the touch location coordinates (x, y) were estimated from the optical response using the touch localisation algorithm. Based on the nominal and estimated coordinates, the root mean square error (RMSE) and the standard deviation σ were calculated. Furthermore, at least 20 measurements were recorded at each location, with the acquisition frame rate determined by the selected sensor operating mode.

As in the FoV assessment procedure, a baseline acquisition was performed prior to the touch localisation evaluation to compensate for ambient light effects.

3.3. Touch localisation algorithm

The individual ToF sample data frame in the light-guide medium can be represented as a two-dimensional matrix $D_f \in \mathbb{R}^{nBeam \times nBin}$. The parameter $nBeam$ denotes the number of beams, corresponding to the vertical superposition of multiple layers of SPAD responses (see Fig. 4). For acrylic glass HardSkin $nBeam = 8$ (8-by-8 mode); for 3D printed HardSkin $nBeam = 7$ (7-by-1 mode); and for soft silicone rubber SoftSkin $nBeam = 4$ (4-by-4 mode).

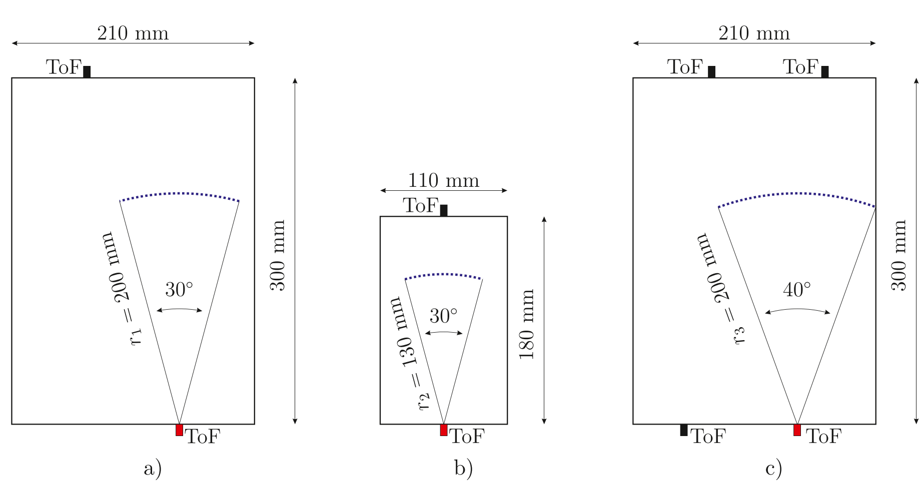

Fig. 6. Touch test points used for the FoV assessment (the ToF sensor under consideration is coloured in red): a) acrylic glass HardSkin, b) 3D-printed HardSkin and c) soft silicone rubber SoftSkin.

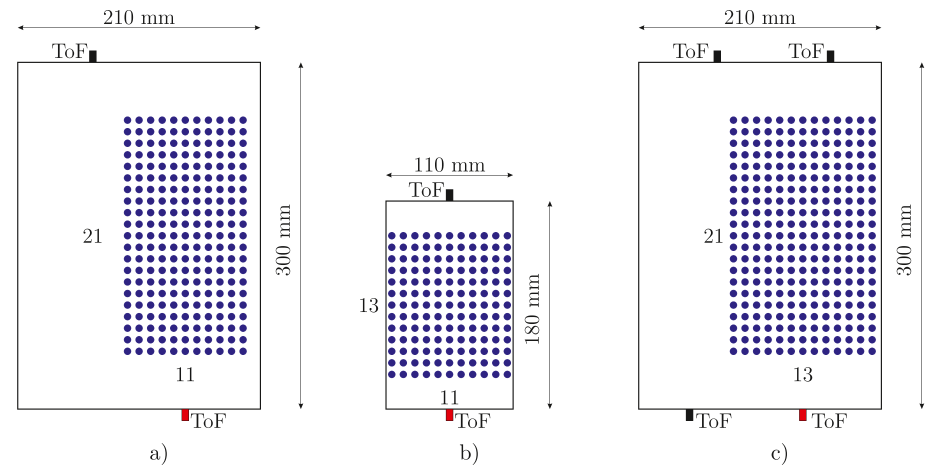

Fig. 7. Rectangular touch grid used for localisation evaluation (the ToF sensor under consideration is coloured in red): a) acrylic glass HardSkin, b) 3D printed HardSkin and c) soft silicone rubber SoftSkin.

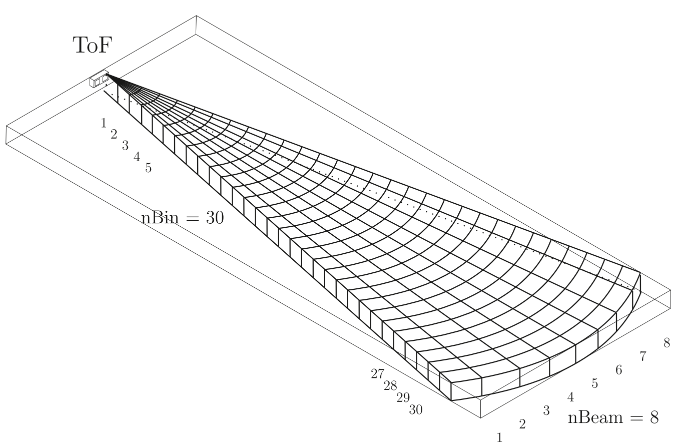

Fig. 8. Data frame D_f representation of the acrylic glass HardSkin as a two-dimensional matrix of histogram data with 30 bins and 8 beams.

The parameter $nBin$ represents the number of range bins from the sensor response and can be interpreted as a maximum sensing radial distance (i.e., the length of the sensing area). Range bins are discrete, uniform distance intervals in the histogram response resulting from TDC. The nominal histogram bin width is stated as $\Delta t = 100$ ps, and the resulting distance resolution equals $\Delta d \approx 15$ mm. Taking into account the refractive index n, the vertical field of view, and the thickness of the prototype, the nominal bin length is 8.9 mm.

In a case of acrylic glass HardSkin and soft silicone rubber SoftSkin, the second dimension of the data frame D_f, $nBin = 30$, and in the case of 3D printed HardSkin $nBin = 18$, since the physical dimensions of the prototype are smaller.

Fig. 8 illustrates the simplified data frame D_f for an acrylic glass HardSkin, with the ToF sensor positioned at the top-left. Bin index values increase with the increasing distance from the sensor (to bottom-right), while beam index values increase from left to right. The data frame representation is not drawn in perspective; in reality, the sensing geometry is conical. It should be noted that the beams are not parallel and become wider with increasing distance from the ToF sensor.

Furthermore, the representation of the data frame D_f can be interpreted as a polar-coordinate heatmap. The beam number corresponds to the discrete angular displacement, while the bin number corresponds to the radial distance from the sensor.

The first step in the localisation algorithm is to determine the corresponding index values $beam_{max}$ and bin_{max} associated with the maximum value D_{max} of a single data frame D_f. These indices represent discrete localisation coordinates in the sensor's local polar coordinate system.

$$D_{max} = \max D_f \tag{1}$$

$$[beam_{max}, bin_{max}] = \arg\max D_f(beam, bin) \tag{2}$$

For interpolation, a 3-by-3 window patch W centred at $(beam_{max}, bin_{max})$ was defined, and the centroid interpolation method was performed (a weighted centre of mass with photon response intensities). Using the proposed method, the calculated indices $beam_i$ and bin_i (where i denotes interpolated values corresponding to the interpolated maximum within W) are no longer restricted to discrete integer values (from $[1, nBeam]$ for beams and $[1, nBin]$ for bins). Instead, $beam_i$ and bin_i may assume continuous values spanning the entire intervals $[0, nBeam]$ and $[0, nBin]$, respectively.

The second step is to assign continuous real-valued estimates of the touch radial distance d (in mm) and the location angle φ (in degrees) from the interpolated values $beam_i$ and bin_i.

$$d = 8.9\ \text{mm} \cdot bin_i \tag{3}$$

$$\varphi = \left(beam_i - \frac{nBeam + 1}{2}\right) \cdot \frac{\Theta_{FoV}}{nBeams} \tag{4}$$

where Θ_{FoV} is obtained from FoV assessment, and 8.9 mm corresponds to the nominal single bin length.

The final step in the localisation algorithm is the conversion from polar coordinates to Cartesian coordinates (based on [18]):

$$x = d \cdot \sin\varphi \tag{5}$$

$$y = d \cdot \cos\varphi \tag{6}$$

Fig. 9 presents a graphical example of a single data frame D_f with the maximum response located at beam 3 and bin 4 (the corresponding beam and bin are highlighted in red). Centred at $(beam_{max}, bin_{max})$, a 3-by-3 window patch W is defined and highlighted in orange.

4. Results

This section presents the results of the experimental evaluation described in the previous section. First, the empirical ToF FoV assessment is discussed, followed by the results of the localisation accuracy evaluation.

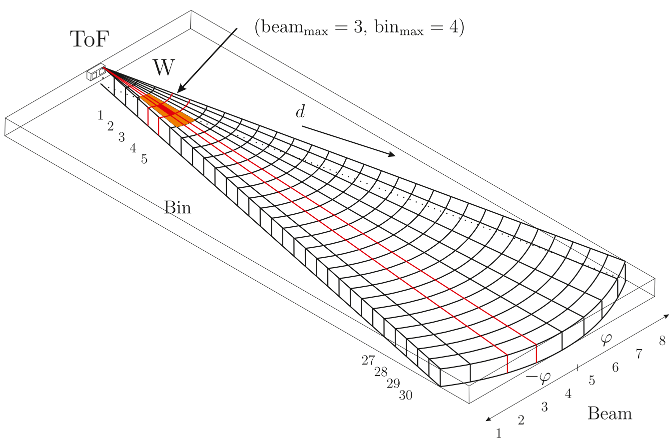

Fig. 9. Example of the touch detection algorithm showing the maximum photon response at beam 3 and bin 4, and a 3-by-3 window patch W centred at $(beam_{max}, bin_{max})$. The variable d denotes the radial distance from the sensor, and φ represents the angular displacement.

Table 2
Nominal (in free space) and experimentally determined beam centres and FoV angle width in ° from FoV assessment for all three OptoSkin prototypes.

Prototype/Beam	1	2	3	4	5	6	7	8	Θ_{FoV}
Nominal values from ToF datasheet:									
Acrylic glass	−17.94	−12.81	−7.69	−2.56	2.56	7.69	12.81	17.94	41
3D printed	−12.43	−8.29	−4.14	−0.00	4.14	8.29	12.43		41
Silicone rubber	−15.38	−5.13	4.13	15.38					41
Experimental results:									
Acrylic glass	−11.4	−8.6	−5.6	−2.0	2.4	4.2	7.2	10.6	28
3D printed	−4.6	−2.4	−1.2	−0.6	0.0	0.2	4.0		29*
Silicone rubber	−14.8	−7.1	5.2	12.2					43

4.1. Empirical FoV assessment

The results of the empirical FoV assessment are summarized in Table 2 and further illustrated in Figs. 10–12.

Table 2 contains the nominal FoV width in free space and calculated data for the actual FoV width Θ_{FoV}, as well as empirically determined centres of beams. The first three rows of the table correspond to the nominal values from the ToF sensor's datasheet for free space for three OptoSkin prototypes. Nominal beam centres are calculated based on the nominal FoV width, accounting for the number of beams. Since the 7-by-1 mode is a custom configuration, its nominal width is not described in a datasheet, but is defined by the SPAD configuration mask (41°). The following rows correspond to the experimental values from the FoV assessment for all three prototypes. The FoV width is defined as the width at which the beam response exceeds the noise level. Beam centres are determined by fitting a Gaussian curve to the beam responses. The number of beams depends on the sensor's operating mode, i.e., the number of beams is 8, 7, or 4.

Specifically, beam responses, represented by the number of detected (i.e., reflected) photons in response to mechanical stimulation at positions along the testing arc, are visualized in Fig. 10 for acrylic glass HardSkin (operating in 8-by-8 mode), in Fig. 11 for 3D-printed HardSkin (operating in 7-by-1 mode), and in Fig. 12 for soft silicone rubber SoftSkin (operating in 4-by-4 mode). The number of reflected photons in response to mechanical stimulation at locations along the testing arc is shown on the vertical axis, whereas the horizontal axis corresponds to the actual angular position on the testing arc during the FoV assessment. Each curve, representing the response of an individual beam, describes the dependence of the number of detected photons (photon count) on the angle of incidence. The vertical dotted lines indicate the beam-center angles, which were experimentally determined as the centers of the best-fit Gaussian curves to the beam responses (as listed in Table 2).

4.2. Localisation accuracy evaluation

Figs. 13–15 present the localisation accuracy results for the sensing area within the ToF sensor FoV. The results for acrylic glass HardSkin are shown in Fig. 13, those for 3D-printed HardSkin in Fig. 14, and those for soft silicone rubber SoftSkin in Fig. 15.

In each of Figs. 13–15, the localisation map is displayed on the left, the RMSE map in the center, and the calculated standard deviation map on the right. In the localisation maps, different colors represent the assessed touch locations corresponding to different nominal touch-point positions. For the RMSE representation (localisation root mean square error between the actual and assessed touch locations), a color map ranging from 0 mm (dark blue) to 20 mm (yellow) is used. For the standard deviation σ, a color map ranging from 0 mm (dark blue) to 5 mm (dark red) is applied.

The RMSE and standard deviation maps are calculated and illustrated for a predefined rectangular grid, indicated by blue circles on the localisation map.

5. Discussion

The presented results demonstrate the capability of touch sensing based on ToF measurements within optically transparent materials, as well as the accuracy of touch location assessment achieved using the proposed OptoSkin sensor surface.

In experiments, the AMS Osram TMF8828 ToF sensor was used in three light-guide medium materials with different optical characteristics. A closer examination of the data in Table 1 reveals a relative similarity in the values of transmittance T and refractive index n across all evaluated materials. In contrast, more pronounced differences are observed in the diffuse reflectance R_d and scattering coefficient μ_s.

The 3D-printed HardSkin (MonoCure3D Pro Crystal Clear 2) exhibits the highest diffuse reflectance R_d, exceeding that of the other two materials by more than a factor of three. In general, lower values of R_d indicate better light transmission. The same trend applies to the scattering coefficient μ_s, where lower values correspond to improved optical performance of the material. Based on these parameters, acrylic glass exhibits higher optical clarity for laser beam transmission.

Aulika et al. [19] performed a direct SNR evaluation for different optical materials and concluded that the acrylic glass and Crystalflex materials consistently deliver high SNR values under FTIR conditions. On the other hand, 3D-printed HardSkin material performs poorly in FTIR measurements due to excessive internal scattering, leading to light loss via angular dispersion.

Fig. 10 presents the beam responses obtained during the acrylic glass HardSkin FoV assessment. A closer examination of the individual beam responses reveals that the maximum responses increase from beam 1 to beam 4, while those from beam 5 to beam 8 gradually decrease. The reduced responses observed in the side beams are consistent with the FoV characteristics reported in the ToF sensor datasheet.

The maximum illumination (at least 90% of the maximum range) is specified for the angular region of ±10°, after which the illumination intensity decreases to 20% or less within the subsequent 5°. The peaks of the individual beam responses are distributed evenly and symmetrically, with only minor deviations observed in the calculated peak positions of Beam 5 and Beam 6.

The FoV angle width Θ_{FoV} is determined based on the noise-level responses of the outer beams. For the acrylic glass HardSkin, the resulting FoV is $\Theta_{FoV} = 28°$, which is smaller than the value specified in the sensor datasheet for free-space operation (41°).

Similar to the acrylic glass HardSkin, Fig. 12 illustrates the beam responses obtained for the soft silicone rubber SoftSkin. In this case, the ToF sensor operates in 4-by-4 mode, providing measurements from

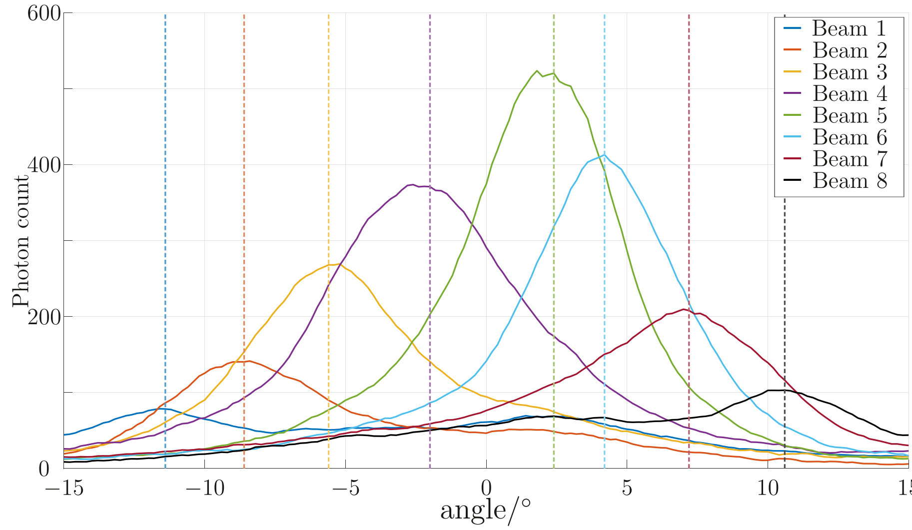

Fig. 10. Beam responses for acrylic glass HardSkin during the FoV assessment. Vertical dotted lines indicate the experimentally determined beam centers.

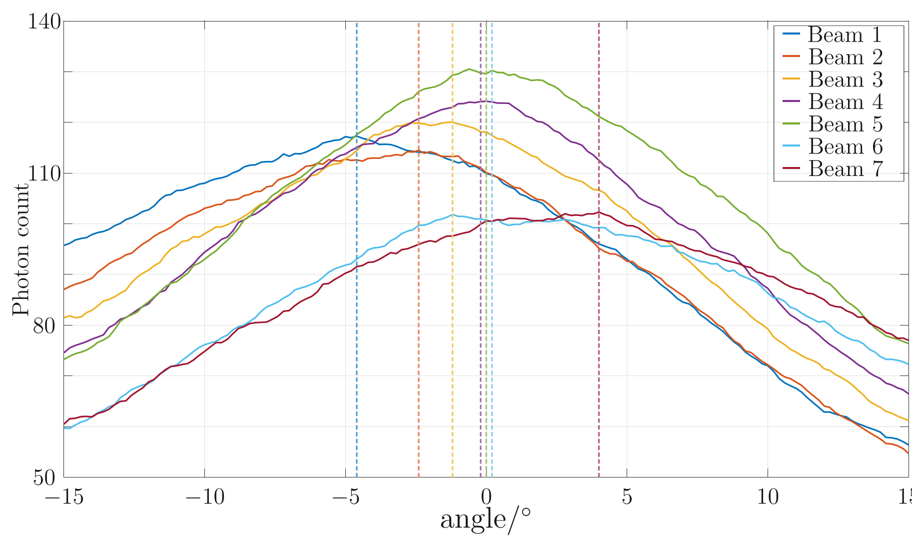

Fig. 11. Beam responses for 3D-printed HardSkin during the FoV assessment. Vertical dotted lines indicate the experimentally determined beam centers.

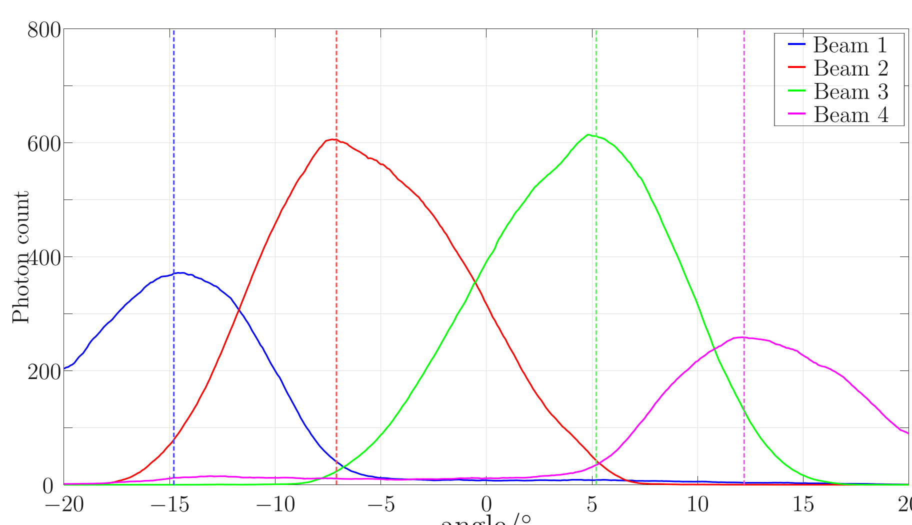

Fig. 12. Beam responses for soft silicone rubber SoftSkin during the FoV assessment. Vertical dotted lines indicate the experimentally determined beam centers.

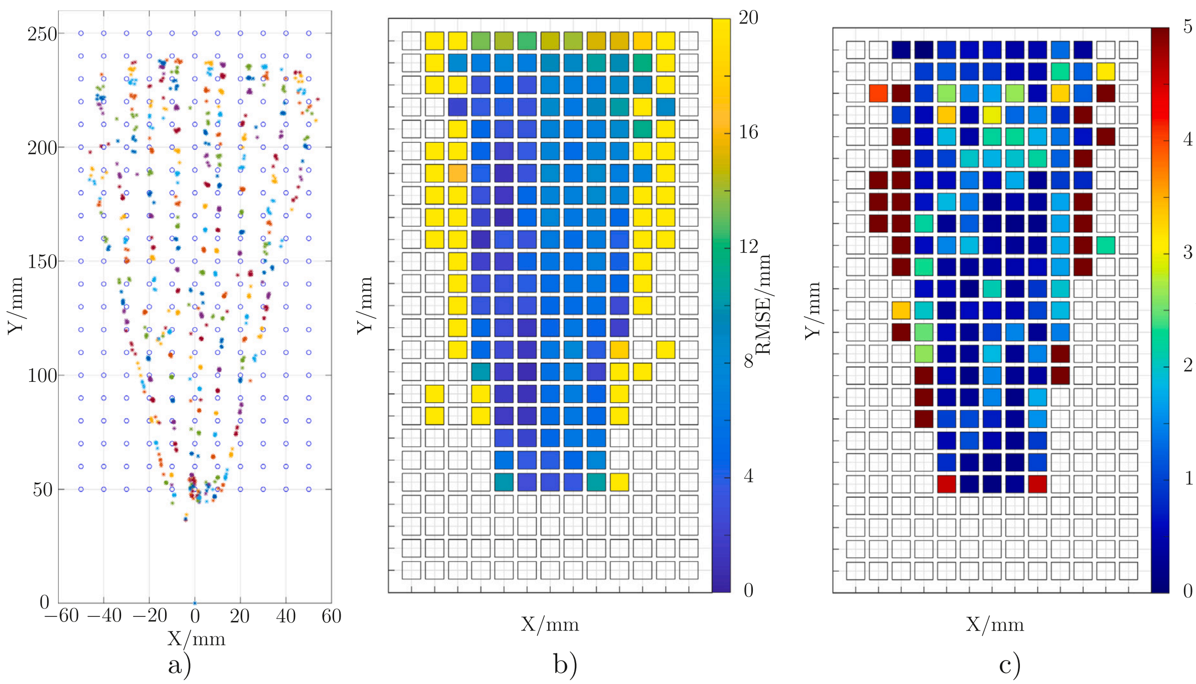

Fig. 13. Acrylic glass HardSkin localisation results: (a) localisation map, (b) RMSE, and (c) standard deviation.

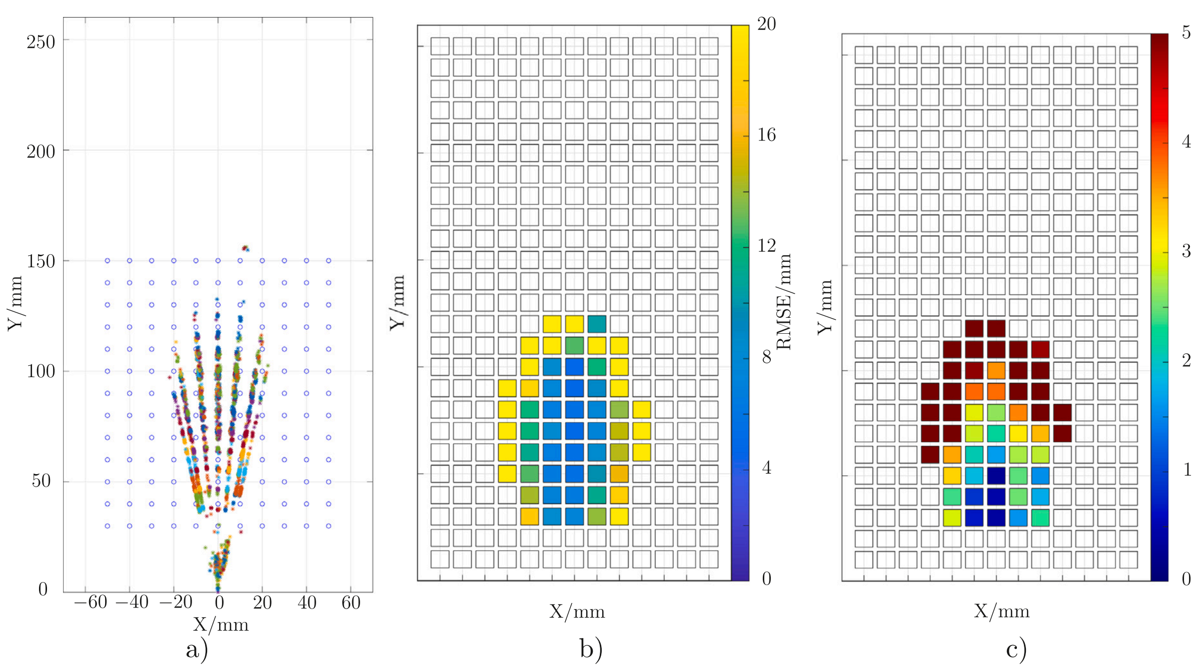

Fig. 14. 3D-printed HardSkin localisation results: (a) localisation map, (b) RMSE, and (c) standard deviation.

four individual beams. As observed previously, the outer beams exhibit lower responses compared to the central beams, which is consistent with the sensor's FoI characteristics described in the previous paragraph. The beam responses are generally symmetrical; however, a slight overall shift toward negative angles is evident, with the intersection between Beam 2 and Beam 3 located at approximately -1°. This shift arises from the definition of the origin of the sensor coordinate system. Furthermore, the measured responses indicate a significantly wider field of view, $\Theta_{FoV} > 40^\circ$, which can be attributed to the deformable nature of the soft silicone surface. When pressure is applied, the surface deforms in the contact region, causing the conditions for TIR to no longer be satisfied and enabling light to be reflected back toward the sensors.

As shown in Fig. 11, the distribution of beam peaks for the 3D-printed HardSkin is less distinct compared to the other two cases. This behavior is primarily attributed to increased light scattering between the layers of the 3D-printed material, which attenuates the detected signal. The scattering coefficient μ_s reported in Table 1 confirms this observation, with the 3D-printed material exhibiting the highest scattering coefficient value ($\mu_s = 0.2$ cm^{-1}). Nevertheless, seven individual beams can still be identified due to the 7-by-1 operating mode. However, their peak

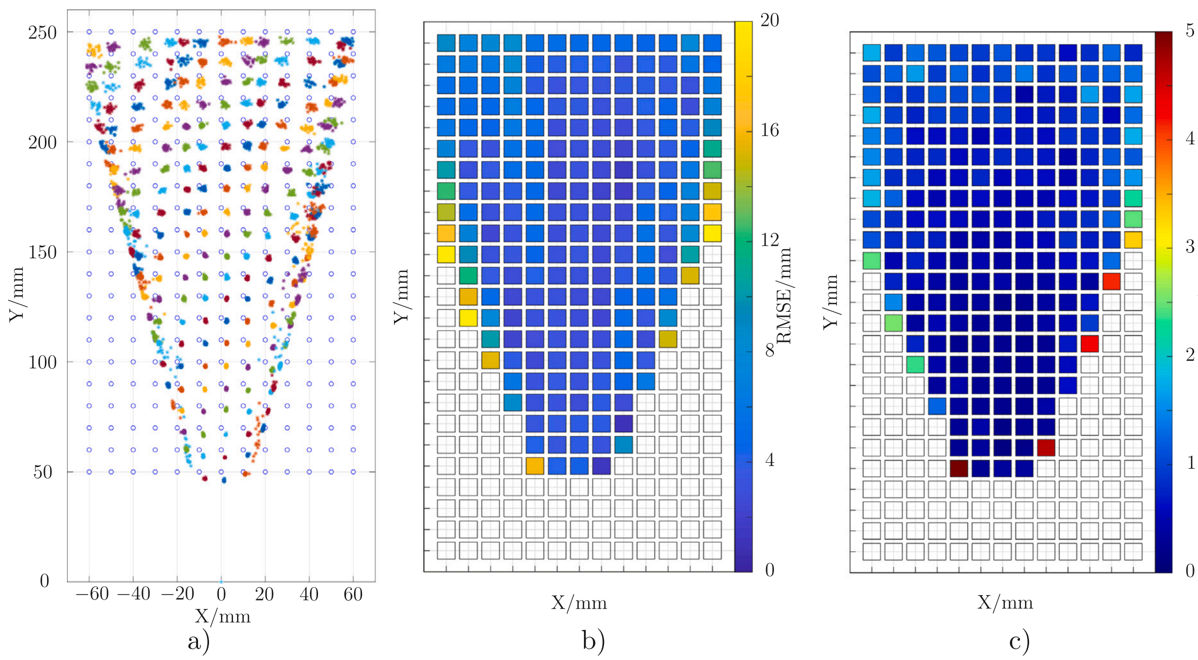

Fig. 15. Soft silicone rubber SoftSkin localisation results: (a) localisation map, (b) RMSE, and (c) standard deviation.

responses are not evenly distributed, in contrast to the more uniform beam spacing observed for the other two materials.

A comparison between the nominal and experimentally determined values in Table 2 highlights the importance of performing an experimental FoV assessment. The parameter Θ_{FoV} is directly used in the localisation algorithm, and an incorrect FoV width leads to inaccurate localisation calculations. The theoretical FoV, using Snell's law, is close to the experimentally obtained results for acrylic glass HardSkin (27.4°). The same calculated value applies to 3D-printed HardSkin. The theoretical FoV for SoftSkin (29.1°) differs from the experimentally obtained value (43°). Applied touches slightly outside the sensor FoV, cause its penetration to deform the soft material. Accordingly, a response can be sensed even with touches outside the sensor's FoV.

The primary focus of the presented analysis is to evaluate the accuracy of touch position sensing on the OptoSkin surface. The key objectives of the study are to compare the root mean square error (RMSE) between the detected and nominal touch positions, as well as the standard deviation σ for each touch location. Figs. 13–15 present the results of the localisation accuracy evaluation. Each figure consists of three subfigures. The left subfigure shows a visualization of the sensed touch points (marked with coloured asterisks) obtained from the OptoSkin prototype, overlaid on a nominal rectangular grid of actual touch locations (denoted by blue circles).

The closer a cluster of points of the same color lies to the corresponding nominal grid point, the smaller the RMSE error (subfigure b). Likewise, the smaller the area occupied by a cluster of points, the lower the variance, that is, the standard deviation (subfigure c).

A visual comparison of the localisation maps for the OptoSkin prototypes in Figs. 13(a), Fig. 14(a), and Fig. 15(a) reveals the closest agreement between the sensed touch positions and the nominal grid points for the soft silicone rubber SoftSkin.

An analysis of the RMSE maps of the sensed touch locations confirms these observations. All RMSE figures use the same color-map range, enabling direct comparison. For both acrylic glass HardSkin and soft silicone rubber SoftSkin, the RMSE remains below 10 mm across most of the sensing area. In contrast, the proportion of the area with an RMSE below 10 mm is significantly smaller for the 3D-printed HardSkin. In all three cases, increased RMSE values are observed near the edges of the FoV. One reason is the interpolation between zones inside and outside the ToF sensor FoV. The other reason is that the amount of reflected light is proportional to the surface area of the contact zone. Near the FoV boundary, not all of the contact zone's surface area is illuminated and sensed. Additionally, for the 3D-printed HardSkin, elevated RMSE is also evident at radial distances greater than 110 mm.

The subfigures illustrating RMSE and standard deviation further confirm these findings, with increased deviations observed toward the edges of the FoV. For the acrylic glass HardSkin, the touch localisation exhibits a relatively uniform standard deviation across the FoV. However, increased variation is observed near the lateral FoV boundaries and at radial distances greater than 200 mm. The 3D-printed HardSkin shows the highest variability in touch localisation, which can be attributed to its layered structure (Fig. 14c). Across most of the FoV, the standard deviation exceeds 2 mm. In contrast, the lowest standard deviation is obtained for the soft silicone rubber SoftSkin (Fig. 15c). Only at certain locations near the FoV edges does the variation exceed 2 mm. For SoftSkin, the standard deviation slightly increases with radial distance from the ToF sensor, yet remains below 2 mm across the majority of the sensing area.

The ToF sensor, and consequently the OptoSkin prototypes, are not resistant to changes in ambient light. Garcia et al. [23] conducted controlled experiments across different spectral ranges, from the visible to the infrared. They observed that the sensor response is not affected even at high ambient brightness (1.2 $\mathrm{mW/cm^2}$) in the visible spectrum. In contrast, the effect is noticeable in the infrared range. As infrared irradiance increases, increasingly severe effects are observed. The increasing infrared light level leads to a flattening of the photon response and the eventual disappearance of the contact signature at an intensity of 1.3 $\mathrm{mW/cm^2}$. With our proposed method, which subtracts the zero (no-contact) state, called the baseline, we mitigate the influence of temporal ambient light. If ambient lighting conditions change significantly during the operation, a baseline acquisition should be re-run. The touch localisation algorithm is based on searching for the distance (corresponding bin) with the highest response in the histogram. Despite ambient light (especially in the infrared spectrum) affecting the photon response intensity, it does not affect the peak location or the subsequent localisation algorithm. Furthermore, significant changes in ambient infrared light are unlikely to occur in real-world indoor scenarios.

The presented work focuses on the planar single-touch localisation performance of three OptoSkin prototypes. By extending the histogram algorithm with multiple-peak detection above a threshold value and incorporating multiple ToF sensors, the presented approach can be extended to multi-touch localisation. The evaluation of the multi-touch localisation performance would require a separate evaluation protocol and further analysis. It is important to note that each (detected) touch "weakens" the photon response for the detection of an additional touch in the same line of sight at a greater distance.

The results of this study demonstrate that accurate touch location sensing within optically transparent media is feasible, with relatively low variation. Overall, the best performance in terms of RMSE and variation is achieved with the soft silicone rubber SoftSkin. The primary reason lies in its operating principle and the light refraction behavior within the soft light-guiding material. When pressure is applied, the material deforms, resulting in increased light refraction back toward the sensor compared to the FTIR-only operating principle. Although acrylic glass exhibits superior optical characteristics compared to transparent silicone (Table 1), the deformation-based sensing responses are significantly more pronounced than those relying solely on the FTIR principle.

6. Conclusion

Integrated laser ToF sensors open new possibilities not only for space and environment perception but also for novel approaches to touch sensing. By exploiting the light-propagation characteristics of optically transparent materials, an optical sensing surface concept, termed OptoSkin, was developed. This work presents an evaluation of touch position detection accuracy for three OptoSkin surface prototypes (acrylic glass, 3D-printed transparent material, and transparent soft silicone rubber) developed within the EU SestoSenso project.

OptoSkin employs the FTIR operational principle for light propagation, with the main advantage being its ability to cover a large sensing area for touch detection without the need to wire individual touch-sensing subregions (taxels).

For automated and repeatable evaluation of touch location accuracy and variation, a robotic test setup was assembled, consisting of an industrial robot, two force–torque sensors, and a specialized tool (indenter). In the first step, the field of view (FoV) was assessed for each prototype to incorporate it into the localisation algorithm. In the second stage, the accuracy of touch location sensing was evaluated using a rectangular grid of nominal touch locations.

The results of the study reveal that the selection of the optical medium material is crucial for the sensing area and touch detection performance of the OptoSkin system. The acrylic glass and transparent soft silicone rubber prototypes enable a sensing range of up to 250 mm with a localisation error below 10 mm. In contrast, the 3D-printed material introduces increased light scattering, which reduces the effective sensing range to approximately 110 mm and results in higher localisation error. Soft silicone rubber OptoSkin shows the best performance, with localisation error less than 5 mm and variance less than 1 mm across the entire FoV.

If the difference in the refractive index (which is small) is ignored, the radial distance resolution is the same for all three prototypes. The main difference among prototypes remains in angular resolution, which is theoretically best for acrylic glass HardSkin ($27.4°/8 \approx 3.4°$), followed by 3D-printed HardSkin ($27.4°/7 \approx 3.9°$), and worst for SoftSkin ($29.1°/4 \approx 7.3°$). Consequently, based on theoretical resolution, we should expect the best localisation results for both HardSkin prototypes; however, this is not the case. The explanation for the different results must lie in the material rather than in the ToF sensor operating mode.

With this study, the feasibility of ToF-based touch detection within an optically transparent medium is confirmed. The results can also serve as a guideline for OptoSkin sensor fabrication. The use of a 3D-printing approach offers the greatest freedom in sensor shape design, while fabrication by casting provides a favourable compromise between geometric flexibility and sensor performance.

CRediT authorship contribution statement

Aleš Zore: Writing – review & editing, Writing – original draft, Validation, Software, Methodology, Investigation, Formal analysis, Data curation, Conceptualization. **Julija Stopar:** Writing – review & editing, Validation, Software, Investigation, Data curation. **Andrejs Ogurcovs:** Writing – review & editing, Validation, Software, Methodology, Conceptualization. **Jelena Butikova:** Writing – review & editing, Validation, Investigation, Formal analysis. **Ilze Aulika:** Writing – review & editing, Supervision, Resources, Project administration, Funding acquisition, Conceptualization. **Jorge Garcia:** Writing – review & editing, Software, Investigation, Conceptualization. **Sergio Cartiel:** Writing – review & editing, Software, Investigation, Conceptualization. **Adolfo Muñoz:** Writing – review & editing, Resources, Project administration, Funding acquisition, Conceptualization. **Martin Laurenzis:** Writing – review & editing, Resources, Project administration, Funding acquisition, Conceptualization. **Emmanuel Bacher:** Writing – review & editing, Software, Investigation, Conceptualization. **Marko Munih:** Writing – review & editing, Supervision, Resources, Project administration, Funding acquisition, Conceptualization. **Roman Kamnik:** Writing – review & editing, Writing – original draft, Supervision, Resources, Project administration, Methodology, Investigation, Funding acquisition, Conceptualization.

Declaration of competing interest

The authors declare that they have no known competing financial interests or personal relationships that could have appeared to influence the work reported in this paper.

Acknowledgements

This work was funded by the European Commission's HORIZON EUROPE Research and Innovation Actions under GA number 101070310 and by Slovenian Research Agency (Funding No. P2-0228).

During the preparation of this work the authors used OpenAI models solely to improve language quality and readability. After using this tool/service, the authors reviewed and edited the content as needed and take full responsibility for the content of the submitted article.

Data availability

Data will be made available upon request.

References

[1] L. Wang, D.J. Beebe, A silicon-based shear force sensor: development and characterization, Sens. Actuators a Phys. 84 (1) (2000) 33–44, https://doi.org/10.1016/S0924-4247(99)00342-8
[2] S. Kimura, K. Nakatsuma, Y. Ohshima, M. Tanabe, M. Kobayashi, I. Torigoe, Fabrication and evaluation of an uniform piezoelectric film for a robot skin sensor, in: 2018 IEEE Sensors, 2018, pp. 1–4, https://doi.org/10.1109/ICSENS.2018.8589605
[3] M. Tanaka, T. Iijima, Y. Tanahashi, S. Chonan, Development of a 3D tactile sensor, J. Mater. Process. Technol., selected Papers from the 4th Japanese-Mediterranean Workshop on Applied Electromagnetic Engineering for Magnetic, Superconducting and Nano Materials. 181 (1) (2007) 286–290, https://doi.org/10.1016/j.jmatprotec.2006.03.059
[4] S. Takenawa, A magnetic type tactile sensor using a two-dimensional array of inductors, in: 2009 IEEE International Conference on Robotics and Automation, 2009, pp. 3295–3300, https://doi.org/10.1109/ROBOT.2009.5152420
[5] C. Lucarotti, C.M. Oddo, N. Vitiello, M.C. Carrozza, Synthetic and bio-artificial tactile sensing: a review, Sensors 13 (2) (2013) 1435–1466, https://doi.org/10.3390/s130201435
[6] W.P. Mark, R. Cutkosky, Handbook of Robotics, second ed, Springer, 2016, Ch. Force and Tactile Sensing.
[7] R.S. Dahiya, G. Metta, M. Valle, G. Sandini, Tactile sensing–from humans to humanoids, IEEE Trans. Robot. 26 (1) (2010) 1–20, https://doi.org/10.1109/TRO.2009.2033627
[8] P. Maiolino, M. Maggiali, G. Cannata, G. Metta, L. Natale, A flexible and robust large scale capacitive tactile system for robots, arXiv preprint arXiv:1411.6837, 2014.

[9] Z. Ji, H. Zhu, H. Liu, T. Chen, L. Sun, A flexible capacitive tactile sensor for robot skin, in: 2016 International Conference on Advanced Robotics and Mechatronics (ICARM), 2016, pp. 207–212, https://doi.org/10.1109/ICARM.2016.7606920

[10] G. Cannata, M. Maggiali, G. Metta, G. Sandini, An embedded artificial skin for humanoid robots, in: 2008 IEEE International Conference on Multisensor Fusion and Integration for Intelligent Systems, 2008, pp. 434–438, https://doi.org/10.1109/MFI.2008.4648033

[11] T.-H.-L. Le, P. Maiolino, F. Mastrogiovanni, G. Cannata, Skinning a robot: design methodologies for large-scale robot skin, IEEE Robotics and Automation Magazine 23 (4) (2016) 150–159, https://doi.org/10.1109/MRA.2016.2548800

[12] K. Keum, et al., Textile-based capacitive pressure sensor array for wearable and robotic applications, Sensors 21 (2) (2021) 442.

[13] F. Xu, et al., A soft omnidirectional capacitive tactile sensor for robotic applications, Biosensors 12 (7) (2022) 506.

[14] S.S. Desai, A.M. Eckert-Erdheim, A.M. Hoover, A large-area tactile force sensor for measuring ground reaction forces from small legged robots, in: 2013 IEEE/RSJ International Conference on Intelligent Robots and Systems, 2013, pp. 4753–4758, https://doi.org/10.1109/IROS.2013.6697041

[15] A.J. Fernandez, H. Weng, P.B. Umbanhowar, K.M. Lynch, Visiflex: a low-cost compliant tactile fingertip for force, torque, and contact sensing, IEEE Robot. Autom. Lett. 6 (2) (2021) 3009–3016, https://doi.org/10.1109/LRA.2021.3061378

[16] R. Wattanaparinton, K. Takemura, Vision-based tactile sensing using multiple contact images generated by re-propagated frustrated total internal reflections, in: 2022 IEEE International Conference on Systems, Man, and Cybernetics (SMC), 2022, pp. 962–967, https://doi.org/10.1109/SMC53654.2022.9945094

[17] J.-T. Lin, C.A. Newquist, C.K. Harnett, Multitouch pressure sensing with soft optical time-of-flight sensors, IEEE Trans. Instrum. Meas. 71 (2022) 1–8, https://doi.org/10.1109/TIM.2022.3141159

[18] E. Bacher, S. Cartiel, J. García-Pueyo, J. Stopar, A. Zore, R. Kamnik, I. Aulika, A. Ogurcovs, J. Grūbe, A. Bundulis, J. Butikova, M. Kemere, A. Muñoz, M. Laurenzis, Optoskin: novel LiDAR touch sensors for detection of touch and pressure within wave guides, IEEE Sens. J. 24 (20) (2024) 33268–33280, https://doi.org/10.1109/JSEN.2024.3443615

[19] I. Aulika, A. Ogurcovs, M. Kemere, A. Bundulis, J. Butikova, K. Kundzins, E. Bacher, M. Laurenzis, S. Schertzer, J. Stopar, A. Zore, R. Kamnik, Influence of material optical properties in direct tof LiDAR optical tactile sensing: comprehensive evaluation, Materials 18 (14) (2025), https://doi.org/10.3390/ma18143287

[20] M. Born, E. Wolf, Principles of Optics: Electromagnetic Theory of Propagation, Interference and Diffraction of Light, Elsevier, 2013.

[21] Z. Denniz, Y. Gandomi, Biomechanical model of human index finger during examination, Journal of Science and Medicine 3 (1) (2020) 1–14, https://doi.org/10.37714/josam.v2i4.51

[22] R. Figueroa-Jacinto, T.J. Armstrong, W. Zhou, Normal force distribution and posture of a hand pressing on a flat surface, J. Biomech. 79 (2018) 164–172, https://doi.org/10.1016/j.jbiomech.2018.08.002

[23] J. Garcia-Pueyo, S. Cartiel, E. Bacher, M. Laurenzis, A. Muñoz, Time-of-flight signal processing for FTIR-based tactile sensors, Opt. Express 33 (18) (2025) 38909–38925, https://doi.org/10.1364/OE.570548